

# Confined Spin Waves in Magnetochiral Nanotubes with Axial and Circumferential Magnetization

Maria Carmen Giordano, Mohammad Hamdi, and Andrea Mucchietto  
*École Polytechnique Fédérale de Lausanne (EPFL), School of Engineering, Institute of Materials,  
Laboratory of Nanoscale Magnetic Materials and Magnonics, 1015 Lausanne, Switzerland*

Dirk Grundler\*  
*École Polytechnique Fédérale de Lausanne (EPFL), School of Engineering, Institute of Materials,  
Laboratory of Nanoscale Magnetic Materials and Magnonics, 1015 Lausanne, Switzerland and  
École Polytechnique Fédérale de Lausanne, School of Engineering,  
Institute of Electrical and Micro Engineering, 1015 Lausanne, Switzerland*  
(Dated: February 1, 2023)

We report experimental studies of spin-wave excitations in individual 22 nm thick  $\text{Ni}_{80}\text{Fe}_{20}$  nanotubes with diameters of about 150 nm. We apply Brillouin light-scattering (BLS) spectroscopy under microwave irradiation and resolve sets of discrete resonances in the center of nanotubes ranging from 2.5 to 12.5 GHz. Comparing to a recent theoretical work and micromagnetic simulations, we identify different characteristic eigenmodes depending on the axial, mixed or vortex configuration. The mixed and vortex states give rise to modes with helical phase profiles substantiating an unusual nature of confined modes attributed to non-reciprocal spin waves. Our findings provide microscopic insight into realistic tubular spin-wave nanocavities and magnetochiral effects for 3D nanomagnonics.

## I. INTRODUCTION

Advances in magnonics fosters new ideas for information processing based on reciprocal and non-reciprocal short-wave magnons [1–3]. They set novel grounds for logic nanoelements which, not relying on charge transport, have the advantage of operating with low energy consumption. Among these elements, three-dimensional (3D) magnetic nanostructures are very promising for achieving high integration density [3–6]. Their potential will materialize only when the underlying spin dynamics is understood [7–9].

Nanotubes (NTs) prepared from ferromagnets represent prototypical 3D nanomagnetic structures [9]. They are extremely versatile as their properties change as a function of, both, their geometrical parameters, namely length, inner and outer radius, [10–12] and their axial, helical or vortex-like magnetic configuration [13, 14]. A curvature-induced magnetochiral field originates from dipole-dipole interaction [15] and can induce non-reciprocal spin-wave dispersion relations in case of cylindrical NTs with nanometric radii and circular cross sections [8, 14, 16–18]. Previous experimental studies based on microtubes prepared from rolled-up ferromagnetic layers [19, 20] have not addressed magnetochiral effects as radii were in the micrometer regime. Ferromagnetic nanotubes were investigated recently, however, with hexagonal cross sections [13, 21–24]. In axially magnetized NTs prepared from magnetically isotropic Ni, a series of spin wave resonances were resolved and classified depending on the number of assumed nodal lines in azimuthal direction [21]. The phase distribution across

the NTs as explored theoretically in Refs. [18, 24] was not discussed. Koerber et al. [23] studied propagating spin waves along a  $\text{Ni}_{80}\text{Fe}_{20}$  (permalloy) NT and reported the asymmetric spin-wave transport originally predicted for the cylindrical NTs. Here, the vortex configuration was induced via a growth-induced magnetic anisotropy and not by the dipolar interaction relevant for the curvature induced non-reciprocity. For the simulations, the authors considered an ideal hexagonal nanotube. They did not take into account symmetry-breaking aspects like slanted end surfaces [25] or vortex-like segments of opposing chirality [26] which occur in real nanotubes. Short-segmented nanotubes might serve as vertical through-chip vias in 3D magnonic device architecture [27].

Here, we investigate spin wave modes in NTs with a hexagonal cross section prepared from permalloy (Py) grown by a recently developed plasma-enhanced atomic layer deposition (PEALD) process [22, 28]. Combining Brillouin Light Scattering (BLS) microscopy [Fig. 1(a)] and micromagnetic simulations, we explore the nature of modes occurring in different magnetic configurations with and without helically magnetized segments. Depending on the applied magnetic field we resolve a multitude of spin-wave branches consistent with performed micromagnetic simulations. The latter ones consider symmetry-breaking irregularities of a real nanotube and allow us to relate simulated spin wave modes with helical phase patterns to the measured branches. The phase patterns substantiate a curvature-induced magnetochiral effect which was predicted first for circular NTs and then for hexagonal cross-sections [24]. We find an unusual nature of confined modes which so far was restricted to magnets with Dzyaloshinskii-Moriya interaction [29, 30] and puts a new spin on 3D nanomagnonics.

---

\* dirk.grundler@epfl.ch

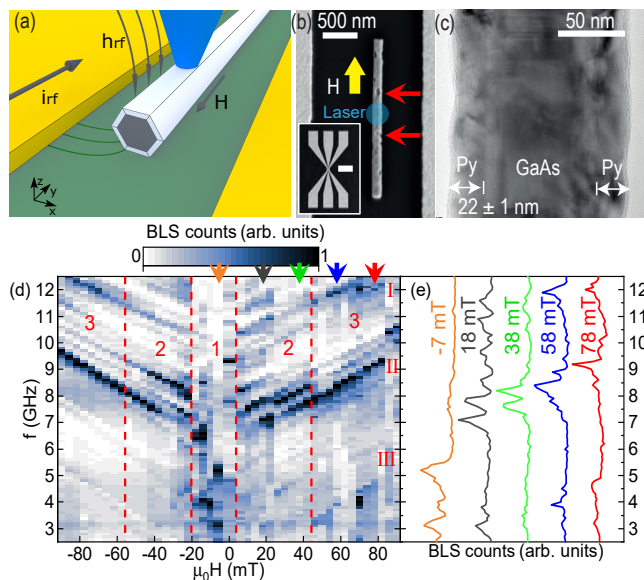


FIG. 1. (a) Sketched excitation-detection scheme based on a coplanar wave guide (CPW) and microfocus Brillouin light scattering microscopy. (b) Scanning electron microscopy image of the nanotube placed parallel to the CPW. The red arrows indicate the nanotrroughs (inset: CPW at a smaller magnification: scale bar:  $200 \mu\text{m}$ ). (c) Transmission electron microscopy image of a Py nanotube on a GaAs core. Shell thickness:  $22 \pm 1 \text{ nm}$ . (d) BLS spectra detected at room temperature at the NT center as a function of field  $H$  applied along the NT axis. Colored arrows indicate fields  $-7$ ,  $18$ ,  $38$ ,  $58$ , and  $78 \text{ mT}$  at which we extract (e) line spectra.

## II. METHODS

### A. Microfocus Brillouin light scattering

The experiments are based on NTs which are positioned in the gap of a coplanar waveguide (CPW) [Fig. 1(a)]. The NTs were obtained through conformal coating of hexagonal semiconductor nanowires (see further details in the Supplemental Material [31] and Refs. [32, 33]). The regular hexagonal cross-section of the nanotemplate covered with a conformal ferromagnetic shell can be seen in Supplementary Fig. S1 (Fig. 1) of Ref. [21] (Ref. [34]). By preliminary magnetization dynamics measurements on films and NTs [22] we have found that the PEALD-grown Py showed a low damping and was magnetically isotropic. Our NTs therefore exhibit a different effective field compared to Ref. 23. An rf-current  $i_{\text{rf}}$  applied to the CPW generates a dynamic magnetic field  $h_{\text{rf}}$ .  $h_{\text{rf}}$  excites spin precession in the adjacent ferromagnetic NT [Fig. 1(b)] at the given frequency  $f$ . Spin-precessional motion is detected for different  $f$  varied from  $2.5$  to  $12.5 \text{ GHz}$  using BLS microscopy ( $\mu$ -BLS) [35, 36] at room temperature. To detect the microwave-stimulated magnon resonances locally, we focus a monochromatic blue laser on the sample's top surface and collect the inelastically scattered light in back-reflection geometry. At

the laser wavelength of  $473 \text{ nm}$ , the penetration depth in Py amounts to about  $10 \text{ nm}$ . Hence the BLS is more sensitive to modes localized on the outer surface.

The investigated samples consist of a  $22 \text{ nm}$ -thick Py shell covering a hexagonal GaAs nanowire core and a  $5 \text{ nm}$  thin spacer layer of  $\text{Al}_2\text{O}_3$  used to separate Py and GaAs. In Fig. 1(c) a transmission electron micrograph of the cross section of a NT from the same batch is shown. For the NT on which we focus here we estimate the effective outer radius to be  $r_o = 80 \text{ nm}$  and the inner radius to be  $r_i = 58 \text{ nm}$  according to Refs. 21 and 28 (results on a further NT are presented in the Supplemental Material [31]). An external magnetic field  $H$  is applied along the NT axis ( $z$ -direction). The position of the BLS laser spot is marked with a blue circle in Fig. 1(b) which is comparable to the diameter of the real laser (about  $400 \text{ nm}$ ). It is positioned in the center of the NT between two nanotrroughs which are separated by  $560 \text{ nm}$ . In our experiments, these nanotrroughs are expected to operate as microwave-irradiated emitters of short-wave magnons [37].

### B. Micromagnetic simulations and comparison with experimental spectra

Micromagnetic simulations have been performed using OOMMF [38] with parameters reported in the Supplemental Material [31]. They provided us with eigenfrequencies extracted from power spectral density (PSD) spectra and spin-precessional motion visualized using Mayavi [39] (see also the videos in the Supplemental Material [31]). We do not compare simulated and measured signal strengths quantitatively. The magnetic pulse in micromagnetic simulations is homogeneous in space, while the field of the CPW is inhomogeneous. This discrepancy makes signal strengths different. The finite penetration depth of the laser is not considered in the simulations. This experimental feature modifies the signal strengths of different modes. It might obscure weak modes and bury them in the finite noise level of the experimental setup. Overall, we expect to detect experimentally the modes with a different amplitude distribution than simulated. Some modes might be missing in the measured spectra. In Ref. [24] a theoretical work is presented which provides further details of modes which occur in long nanotubes with different magnetization configurations.

## III. FIELD DEPENDENCY OF SPIN-WAVE SPECTRA

In Fig. 1(d) (Fig. S3) we show the field-dependent BLS spectra detected for sample NT-s1 (NT-s2) under microwave irradiation for which we varied the frequency between  $2.5$  and  $12.5 \text{ GHz}$ . The data were acquired for static fields  $\mu_0 H$  changing from  $+90 \text{ mT}$  to  $-90 \text{ mT}$ . To

display them, we use the scientific colour maps developed by Cramer *et al.* [40] and prevent visual distortion of the data and exclusion of readers with colour-vision deficiencies [41]. Colored arrows on the top indicate the specific fields for which spectra are displayed in Fig. 1(e). Several branches of distinguished eigenmodes are resolved. The Py NTs investigated here show richer spectra compared to the recently studied Ni NTs [21]. We attribute this observation to the improved damping parameter  $\alpha_{\text{Py}} = 0.013$  of the PEALD-grown Py [22] compared to  $\alpha_{\text{Ni}} = 0.045$  for PEALD-grown Ni [28]. The spectra reported here are also richer compared to Py disks [42] and Py rings [43].

The main identified resonance modes show nearly linear dependencies of  $f$  on  $H$  for  $|\mu_0 H| \geq 42$  mT, i.e., in field regime 3 of Fig. 1(d). We categorize the observed branches in three groups I, II, and III by which we subdivide the frequency regime from 2.5 to 12.5 GHz into three parts. When reducing the field below +42 mT, we notice an increase of intensity (dark color) for certain branches near 8 GHz (group II), suggesting a change in the magnetic configuration when entering field regime 2. Similar behavior is observed for the spectra detected in the regime 2 at negative magnetic fields. In field regime 1 at negative fields, strong resonances (dark color) occur at low  $f$  down to about 2.5 GHz and at large  $f$  of about 9 GHz. Together with the lack of mirror symmetry with respect to  $\mu_0 H = 0$ , these resonances indicate the irreversible reversal process of the nanotube near  $H = 0$ .

Our simulations (shown in the Supplemental Material) indicate that a vortex configuration is formed near zero field. The low resonance frequencies in regime 1 are consistent with such a magnetic state. Considering the pronounced intensity of branches near 8 GHz in regime 2, a large part of the NT exhibits a reversed magnetization at -18 mT when coming from positive  $H$ . In Ref. 14, the authors predicted small (large) resonance frequencies for non-reciprocal spin waves in a vortex (axial) magnetic configuration of a circular NT at zero (large) magnetic field, in agreement with the frequency variation of branches observed in Fig. 1(d).

#### IV. SPIN-WAVE CONFINEMENT AND MAGNETIC CONFIGURATIONS IN A REAL NANOTUBE

The richness of the spectra and the resonant modes in group III at large  $H$  in Figs. 1(d) and S3 suggest that not only azimuthal, but also longitudinal confinement is relevant. For the latter aspect, it is reasonable to assume that the nanotranches in the NTs either provide confining boundaries like antidots [44] or act as spin-wave emitters which are coherently excited by the global microwave field of the CPW [37] and thereby induce interference patterns (standing spin waves) between pairs of nanotranches [45]. These assumptions motivated us to perform simulations on an irregularly defined NT segment

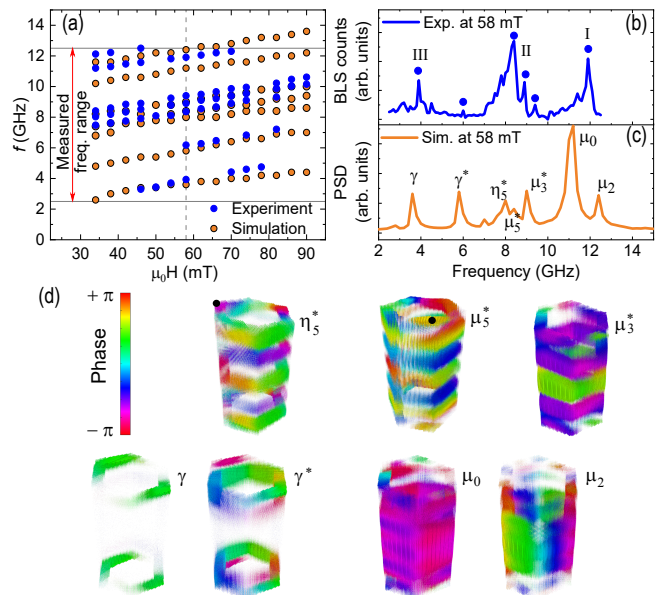


FIG. 2. (a) Eigenmode frequencies detected by  $\mu$ BLS in the central part of a Py NT (blue circles) and simulated resonance frequencies (orange circles) plotted as a function of the magnetic field inducing an axial magnetic state. (b) BLS spectrum and (c) simulated spectrum obtained for a field of 58 mT. Principal eigenmodes are labeled by different letters and correspond to dynamic magnetization profiles in (d). The size of the dots represent the amplitude. The color bar represents spin wave phase ranging from  $-\pi$  to  $+\pi$ .

instead of an infinitely long NT as was done previously. We hence performed simulations of an (approximately) 560-nm-long hexagonal nanotube with slanted edges [31]. These end facets were not parallel and designed such that the finite-sized NT segment had slightly different lengths  $L'$  and  $L''$  on different sides ( $L' > L''$ ). With the help of the static micromagnetic simulations (shown in Fig. S4) we attribute the field regions 1, 2, and 3 to three distinctly different configurations of the NT magnetization  $\mathbf{M}$ . Coming from large positive  $H$ , simulations predict an axial (saturated) state (region 3), a mixed state without (region 2) and with (region 1) a Néel-type domain wall (DW), respectively. In regions 2 and 1, parts of the NTs are in a helical magnetic configuration. In the following we compare dynamic simulations in different regions to experimental BLS spectra and report the emergence of helical spin-wave modes.

##### A. Spin waves in the axially magnetized configuration

It is instructive to first discuss the axial state at large positive fields. In our analysis we consider prominent peaks and the frequency regime between 2.5 and 12.5 GHz covered by the BLS experiment. In Fig. 2(a) we summarize resonance frequencies extracted from  $\mu$ -BLS

between nanotroughs of Py NT-s1 (blue circles) and the simulated resonance frequencies (orange circles) plotted as a function of  $H$ . Experimentally determined resonance frequencies match well with simulated ones (see also Fig. S5). Representative spectra are displayed for 58 mT in Fig. 2(b) and (c) for the experiment and the simulation, respectively. In Fig. 2(b) labels I, II, and III are according to the groups of resonances defined in Fig. 1(d). In Fig. 2(c) the Greek symbols refer to the dynamic magnetization profiles (mode patterns) shown in Fig. 1(d) which are representative for all the fields of the axial (saturated) magnetic state. In the following we discuss the frequency values of resonant modes, and do not refer to the predicted intensities as the selectivity of the BLS microscope concerning specific mode patterns has not been simulated. We follow the nomenclature for modes introduced in Ref. [46]. Simulated modes  $\mu_0$  and  $\mu_2$  occurring at 11.2 and 12.4 GHz, respectively, belong to group I. The mode profile  $\mu_0$  (Fig. 2(d) and Supplemental Movie1 in the Supplemental Material [31]) corresponds to an in-phase spin precession, which is nearly uniform across the NT and can be considered as the ferromagnetic resonance (FMR) with a total wave vector  $k = \sqrt{k_z^2 + k_\varphi^2} = 0$ , where  $\mathbf{k}_z$  ( $\mathbf{k}_\varphi$ ) denote wave vectors in  $\mathbf{z}$  (azimuthal) direction [14]. For spin waves with non-zero wave vector, the finite length and circumference of the nanotube impose a quantization condition on  $k_z$  and  $k_\varphi$ , respectively. The quantization condition for  $k_z$  ( $k_\varphi$ ) reads  $k_z = k_{z,m} = m\pi/L$  ( $k_\varphi = k_{\varphi,\nu} = \nu \times 2\pi/C$ ). We therefore rewrite the total wave vector  $\mathbf{k} = \mathbf{k}_{m\nu} = \mathbf{k}_{z,m} + \mathbf{k}_{\varphi,\nu}$ . The mode  $\mu_2$  illustrates an azimuthal spin wave (Supplemental Movie2 [31]) with total wave vector  $k_{02}$ , i.e.  $k_z = 0$  and  $k_\varphi = 2 \times 2\pi/C = 26.2 \text{ rad}/\mu\text{m}$ .  $\nu$  counts the periods in azimuthal ( $\varphi$ ) direction [24].  $C = 480 \text{ nm}$  is the circumference of the hexagonal NT as defined in Ref. 21. Considering  $\mathbf{k}_\varphi \perp \mathbf{M}$ , the mode reflects the Damon-Eshbach (DE) configuration. Consistent with Ref. [24], its frequency is larger than the FMR. We note that clockwise and counterclockwise azimuthal modes with  $\nu \neq 0$  are split in eigenfrequency by the topological Aharonov-Bohm effect and a standing wave is not formed in azimuthal direction [18, 24].

Simulated modes labeled as  $\mu_3^*$ ,  $\mu_5^*$  and  $\eta_5^*$  have eigenfrequencies of 9, 8.4 and 8 GHz, respectively, consistent with group II resonances. The mode profile of  $\mu_3^*$  agrees with a standing wave confined along a fixed length  $L$ , i.e.  $k_{m\nu} = k_{m0}$ , with a non-zero  $k_z = m\pi/L$  where  $m = 1, 2, \dots$  and  $\nu = 0$ . In this case,  $\mathbf{k}_z$  is parallel to  $\mathbf{M}$  consistent with a backward volume magnetostatic spin wave (BVMSW) configuration. Such modes do not have a pronounced non-reciprocity in axially magnetized NTs [14]. Hence, in Fig. 2(d) (see Supplemental Movie3 [31]), the profile  $\mu_3^*$  incorporates two nearly parallel nodal lines. In Fig. 2(d) the mode profiles of  $\mu_5^*$  and  $\eta_5^*$  are rotated to position in each case the facet with the predominant spin-precessional amplitude on the right side (The profile of  $\eta_5^*$  was rotated by  $120^\circ$  anticlockwise around the  $\mathbf{z}$ -axis

with respect to the profile of  $\mu_5^*$ ). The same corners are marked with black circles. We find that the mode profiles  $\mu_5^*$  and  $\eta_5^*$  represent standing waves with  $m = 5$  confined along facets of different lengths  $L'$  and  $L''$ , respectively (see Supplemental Movie4 and Movie5 [31]). The different longitudinal confinement explains the discrepancy in frequency. The modes labeled  $\gamma$  and  $\gamma^*$  belong to group III with resonant frequencies 3.6 and 5.8 GHz, respectively (see Supplemental Movie6 and Movie7 [31]). Here, spin precession occurs right at the NT edges. Such edge modes [47] have the lowest frequencies due to the demagnetizing effect and small internal fields at edges and the nanotroughs [48]. The fundamental and first higher order edge mode with larger  $k_z$  are separated by about 2.2 GHz which we attribute mainly to exchange interaction.

## B. Spin waves in the mixed state with end vortices

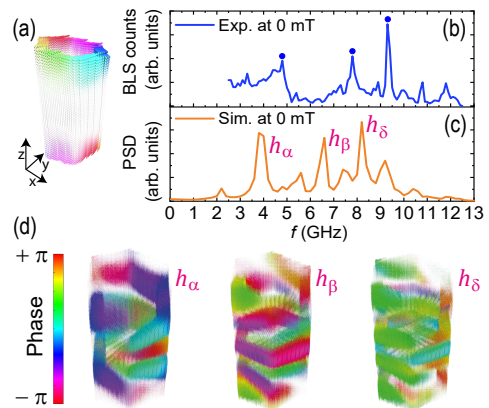


FIG. 3. (a) Simulated static magnetization profile of the NT at  $\mu_0 H_z = 0 \text{ mT}$ . (b) NT-s1 BLS spectrum and (c) simulated spectrum at 0 mT. Specific eigenmodes are labeled by  $h_\alpha$ ,  $h_\beta$ , and  $h_\delta$  and tentatively attributed to modes marked by dots in (b). (d) Dynamic magnetization profiles of modes defined in (c). The size of the dots represent the amplitude. The color bar represents spin wave phase ranging from  $-\pi$  to  $+\pi$ .

As  $H$  is reduced, the mixed state is formed with magnetization vortices of opposite chirality at the ends of the simulated NT and neighboring helically aligned segments [Fig. 3(a)]. Following Ref. 14, NT segments with a circumferential, i.e., helical (vortex) magnetic configuration support non-reciprocal spin waves for non-zero  $k$  ( $k_z$ ). This non-reciprocity has the same origin as in the case of the azimuthal modes in the longitudinally saturated state, i.e., the localization of DE-type modes on either inner or the outer nanotube surface where demagnetizing dynamic fields differ because of different curvatures. The measured (simulated) spectrum at zero field is shown in Fig. 3(b) [Fig. 3(c)]. Simulated phase distributions are shown in Fig. 3(d). Mode  $h_\alpha$  shown in Fig. 3(d) (Supplemental Movie8 [31]) derives most probably from the low-frequency edge mode discussed before.

When extending into the helically aligned center region, the mode exhibits a complex helical phase pattern as non-reciprocal spin waves can not form the regular standing wave patterns [29]. Modes  $h_\beta$  and  $h_\delta$  (see Supplemental Movie9 and Movie10 [31]) reside at higher  $f$  suggesting a larger  $k_z$ . Different from mode  $\mu_3^*$  of the axially aligned state, regular phase patterns with nearly parallel nodal lines are not retrieved in the helical state.

Comparing simulated and experimental spectra in Fig. 2 and Fig. 3, we observe an overall discrepancy of approximately 1 GHz between prominent peaks in measured (indicated by dots) and simulated (indicated by labels) spectra. We explain the discrepancy with the geometry of the real NT which extends beyond the nanotroughs, leading to an overall smaller demagnetization effect compared to the simulated NT. The latter one has hence a smaller internal field, i.e., smaller eigenfrequencies [48] than the measured NT.

### C. Spin waves in the mixed state incorporating a central domain wall

We now discuss spin waves in the mixed state at  $\mu_0 H_z = -14$  mT in which a central DW is assumed [Fig. 4(a)]. The simulation shows two end vortices of opposite chirality which extend to the center. Their circumferential magnetization configurations meet in a Néel-type DW (white region). The detected BLS spectrum at -14 mT is reported in Fig. 4(b) and contains at least three groups of peaks near 4, 6.5 and 8.5 GHz. In the simulated spectrum [Fig. 4(c)] also different groups are identified which we label by d, m and v, respectively. In each group a peak is selected (marked with a black tick at the bottom). The corresponding phase pattern and amplitude profile are displayed in Fig. 4(d) and (e), respectively. The amplitudes are extracted along a line in  $z$ -direction. Vertical dashed lines indicate the width of the DW located near  $z = 280$  nm. The simulated low frequency resonance at 2 GHz (just below the BLS detection window) is attributed to a DW resonance with weak excitation outside (d-mode, Supplemental Movie11 [31]). At 6.6 GHz we find spin-precessional motion with nodes outside the DW (m-mode, Supplemental Movie12 [31]). This mode thereby exhibits a non-zero  $k_z$  within the vortex region. The corresponding DE configuration explains the increased frequency. In the following we select one specific example for a v-mode. At 8.6 GHz (Supplemental Movie13 [31]) we extract six clearly defined nodes along the NT, i.e.,  $m = 7$ , giving rise to a large  $k_z$ . The corresponding wavelength amounts to 160 nm and is in the dipole-exchange regime of spin waves. Analyzing the phase profile in Fig. 4(d) we find that nodal lines at 8.6 GHz have again a chiral appearance, consistent with the predicted asymmetric spin-wave dispersion relations.

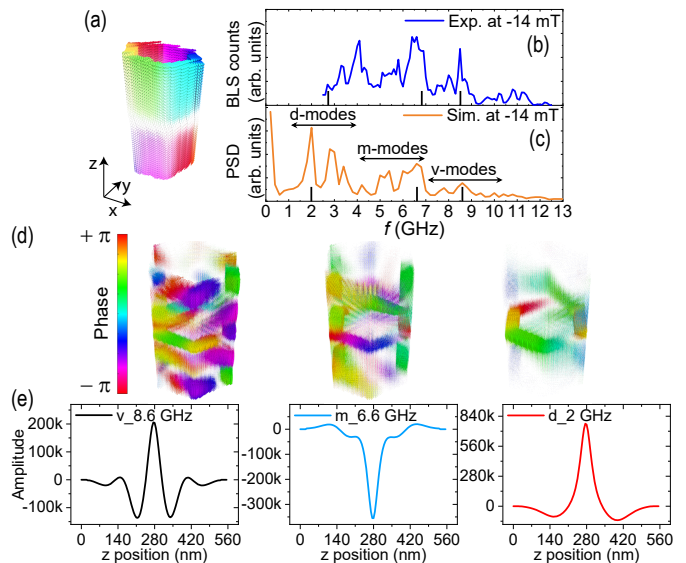


FIG. 4. (a) Simulated static magnetization profile of the NT at  $\mu_0 H_z = -14$  mT. (b) BLS and (c) simulated spectrum at  $\mu_0 H_z = -14$  mT. Eigenmodes in (c) are subdivided in three groups d, m and v. Black ticks refer to mode profiles and amplitudes displayed in (d) and (e), respectively. The size of the dots represent the amplitude. The color bar represents spin wave phase ranging from  $-\pi$  to  $+\pi$ . (e) Spin-precessional amplitudes are plotted along  $z$  for a fixed position in the  $x$ - $y$  plane of the NT.

## V. CONCLUSIONS AND REMARKS

In summary, we detected spin waves in permalloy nanotubes using microfocus BLS. The observed low-frequency resonances were in contrast to theoretical predictions for straight and infinitely long nanotubes. This discrepancy and the observation of unintentional nanotroughs in the real nanotubes motivated us to compare the detected spectra with simulations considering a nanotube segment with slanted edges. Based on the micromagnetic simulations, the rich experimental spectra of eigenmodes were then attributed to spin waves fulfilling interference conditions along both the azimuthal and axial directions of the NT. In the axial magnetic state, nodal lines were found to be mainly straight along the circumference. For helical and vortex-like magnetization orientations, however, nodal lines were distorted which we attribute to the magnetochiral field predicted for nanometric ferromagnetic nanotubes. We hence observe an unusual nature of confined modes reminiscent of magnets subject to Dzyaloshinskii-Moriya interaction. Our findings pave the way for magnetochiral magnonics which is based on 3D device architectures incorporating segments of nanotubular geometry with different magnetic states.

## ACKNOWLEDGMENTS

We thank Didier Bouvet, Anna Fontcuberta i Morral, Gözde Tütüncüoğlu, and Sho Watanabe for support and SNSF for funding via grants 177550 and 197360. M.C. Giordano and M. Hamdi contributed equally to this work.

- 
- [1] V. V. Kruglyak, S. O. Demokritov, and D. Grundler, *J. Phys. D: Appl. Phys.* **43**, 264001 (2010).
- [2] K. Vogt, F. Fradin, J. Pearson, T. Sebastian, S. Bader, B. Hillebrands, A. Hoffmann, and H. Schultheiss, *Nature Communication* **5**, 3727 (2014).
- [3] G. Gubbiotti, *Three-Dimensional Magnonics: Layered, Micro- and Nanostructures; 1st ed* (Jenny Stanford Publishing., 2019).
- [4] S. Sahoo, A. May, A. van Den Berg, A. K. Mondal, S. Ladak, and A. Barman, *Nano Letters* **21**, 4629 (2021).
- [5] S. Sahoo, S. Mondal, G. Williams, A. May, S. Ladak, and A. Barman, *Nanoscale* **10**, 9981 (2018).
- [6] S. S. P. Parkin, M. Hayashi, and L. Thomas, *Science* **320**, 190 (2008).
- [7] P. Fischer, D. Sanz-Hernández, R. Streubel, and A. Fernández-Pacheco, *APL Materials* **8**, 10701 (2020).
- [8] R. Streubel, P. Fischer, F. Kronast, V. P. Kravchuk, D. D. Sheka, Y. Gaididei, O. G. Schmidt, and D. Makarov, *J. Phys. D: Appl. Phys.* **49**, 363001 (2016).
- [9] A. Fernández-Pacheco, R. Streubel, O. Fruchart, R. Hertel, P. Fischer, and R. P. Cowburn, *Nat. Commun.* **8**, 15756 (2017).
- [10] H. Leblond and V. Veerakumar, *Phys. Rev. B* **70**, 134413 (2004).
- [11] J. Escrig, J. Bachmann, J. Jing, M. Daub, D. Altbir, and K. Nielsch, *Phys. Rev. B* **77**, 214421 (2008).
- [12] P. Landeros, O. J. Suarez, A. Cuchillo, and P. Vargas, *Phys. Rev. B* **79**, 024404 (2009).
- [13] D. Ruffer, R. Huber, P. Berberich, S. Albert, E. Russo-Averchi, M. Heiss, J. Arbiol, A. Fontcuberta i Morral, and D. Grundler, *Nanoscale* **4**, 4989 (2012).
- [14] M. M. Salazar-Cardona, L. Körber, H. Schultheiss, K. Lenz, A. Thomas, K. Nielsch, A. Kákay, and J. A. Otálora, *Applied Physics Letters* **118**, 262411 (2021).
- [15] R. Hertel, *SPIN* **03**, 1340009 (2013).
- [16] J. A. Otálora, M. Yan, H. Schultheiss, R. Hertel, and A. Kákay, *Phys. Rev. Lett.* **117**, 227203 (2016).
- [17] J. A. Otálora, M. Yan, H. Schultheiss, R. Hertel, and A. Kákay, *Phys. Rev. B* **95**, 184415 (2017).
- [18] M. Yang, B. Yin, Z. Li, X. Zeng, and M. Yan, *Phys. Rev. B* **103**, 094404 (2021).
- [19] F. Balhorn, S. Jeni, W. Hansen, D. Heitmann, and S. Mendach, *Appl. Phys. Lett.* **100**, 222402 (2012).
- [20] F. Balhorn, C. Bausch, S. Jeni, W. Hansen, D. Heitmann, and S. Mendach, *Phys. Rev. B* **88**, 054402 (2013).
- [21] M. C. Giordano, K. Baumgaertl, S. Escobar Steinvall, J. Gay, M. Vuichard, A. Fontcuberta i Morral, and D. Grundler, *ACS Applied Materials & Interfaces* **12**, 40443 (2020).
- [22] M. C. Giordano, S. Escobar Steinvall, S. Watanabe, A. Fontcuberta i Morral, and D. Grundler, *Nanoscale* **13**, 1351 (2021).
- [23] L. Körber, M. Zimmermann, S. Wintz, S. Finizio, M. Kronseder, D. Bougeard, F. Dirnberger, M. Weigand, J. Raabe, J. A. Otálora, H. Schultheiss, E. Josten, J. Lindner, I. Kézsmárki, C. H. Back, and A. Kákay, *Phys. Rev. B* **104**, 184429 (2021).
- [24] L. Körber, I. Kézsmárki, and A. Kákay, *Phys. Rev. B* **105**, 184435 (2022).
- [25] A. Mehlin, B. Gross, M. Wyss, T. Schefer, G. Tütüncüoğlu, F. Heimbach, A. Fontcuberta i Morral, D. Grundler, and M. Poggio, *Phys. Rev. B* **97**, 134422 (2018).
- [26] M. Wyss, A. Mehlin, B. Gross, A. Buchter, A. Farhan, M. Buzzi, A. Kleibert, G. Tütüncüoğlu, F. Heimbach, A. Fontcuberta i Morral, D. Grundler, and M. Poggio, *Phys. Rev. B* **96**, 024423 (2017).
- [27] A. V. Chumak, P. Kabos, M. Wu, C. Abert, C. Adelman, A. O. Adeyeye, J. Åkerman, F. G. Aliev, A. Anane, A. Awad, C. H. Back, A. Barman, G. E. W. Bauer, M. Becherer, E. N. Beginin, V. A. S. V. Bitencourt, Y. M. Blanter, P. Bortolotti, I. Boventer, D. A. Bozhko, S. A. Bunyaev, J. J. Carmiggelt, R. R. Cheenikundil, F. Ciubotaru, S. Cotozana, G. Csaba, O. V. Dobrovolskiy, C. Dubs, M. Elyasi, K. G. Fripp, H. Fulara, I. A. Golovchanskiy, C. Gonzalez-Ballester, P. Graczyk, D. Grundler, P. Gruszecki, G. Gubbiotti, K. Guslienko, A. Haldar, S. Hamdioui, R. Hertel, B. Hillebrands, T. Hioki, A. Houshang, C.-M. Hu, H. Huebl, M. Huth, E. Iacocca, M. B. Jungfleisch, G. N. Kakazei, A. Khitun, R. Khymyn, T. Kikkawa, M. Kläui, O. Klein, J. W. Klos, S. Knauer, S. Koraltan, M. Kostylev, M. Krawczyk, I. N. Krivorotov, V. V. Kruglyak, D. Lachance-Quirion, S. Ladak, R. Lebrun, Y. Li, M. Lindner, R. Macêdo, S. Mayr, G. A. Melkov, S. Mieszczak, Y. Nakamura, H. T. Nembach, A. A. Nikitin, S. A. Nikitov, V. Novosad, J. A. Otálora, Y. Otani, A. Papp, B. Pigeau, P. Pirro, W. Porod, F. Porrati, H. Qin, B. Rana, T. Reimann, F. Riente, O. Romero-Isart, A. Ross, A. V. Sadovnikov, A. R. Safin, E. Saitoh, G. Schmidt, H. Schultheiss, K. Schultheiss, A. A. Serga, S. Sharma, J. M. Shaw, D. Suess, O. Surzhenko, K. Szulc, T. Taniguchi, M. Urbánek, K. Usami, A. B. Ustinov, T. van der Sar, S. van Dijken, V. I. Vasyuchka, R. Verba, S. V. Kusminskiy, Q. Wang, M. Weides, M. Weiler, S. Wintz, S. P. Wolfski, and X. Zhang, *IEEE Transactions on Magnetics* **58**, 1 (2022).
- [28] M. C. Giordano, *Atomic layer deposition of Ni and Ni<sub>80</sub>Fe<sub>20</sub> for tubular spin-wave nanocavities*, PhD thesis, EPFL (2021).

- [29] B. W. Zingsem, M. Farle, R. L. Stamps, and R. E. Camley, *Phys. Rev. B* **99**, 214429 (2019).
- [30] P. Che, I. Stasinopoulos, A. Mucchietto, J. Li, H. Berger, A. Bauer, C. Pfeleiderer, and D. Grundler, *Phys. Rev. Research* **3**, 033104 (2021).
- [31] See Supplemental Material. In the supplemental movies (a) represent the spin wave profile across a cross sectional cut at the represented height of the NT and (b) shows the spin wave profile on the entire NT while NT is rotating along its axis. The spin wave amplitude is represented by size of the dots. The color bar represents spin wave phase ranging from  $-\pi$  to  $+\pi$ . Supplemental movies are prepared using Mayavi [39].
- [32] F. Matteini, G. Tütüncüoğlu, D. Mikulik, J. Vukajlović-Plestina, H. Potts, J.-B. Leran, W. C. Carter, and A. Fontcuberta i Morral, *Crystal Growth & Design* **16**, 5781 (2016).
- [33] A. P. Chen, J. M. Gonzalez, and K. Y. Guslienko, *J. Appl. Phys.* **109**, 073923 (2011).
- [34] D. Rüffer, M. Slot, R. Huber, T. Schwarze, F. Heimbach, G. Tütüncüoğlu, F. Matteini, E. Russo-Averchi, A. Kovács, R. Dunin-Borkowski, R. R. Zamani, J. R. Morante, J. Arbiol, A. Fontcuberta i Morral, and D. Grundler, *APL Mater.* **2**, 076112 (2014).
- [35] S. O. Demokritov and V. E. Demidov, *IEEE Trans. Magn.* **44**, 6–12 (2008).
- [36] T. Sebastian, K. Schultheiss, B. Obry, B. Hillebrands, and H. Schultheiss, *Frontiers in Physics* **3**, 35 (2015).
- [37] C. S. Davies, A. V. Sadovnikov, S. V. Grishin, Y. P. Sharaevskii, S. A. Nikitov, and V. V. Kruglyak, *Appl. Phys. Lett.* **107**, 162401 (2015), <https://doi.org/10.1063/1.4933263>.
- [38] M. J. Donahue and D. G. Porter, *OOMMF user's guide, version 1.0* (US Department of Commerce, National Institute of Standards and Technology, 1999).
- [39] P. Ramachandran and G. Varoquaux, *Computing in Science & Engineering* **13**, 40 (2011).
- [40] F. Cramer, Zenodo 10.5281/ZENODO.5501399.
- [41] F. Cramer, G. E. Shephard, and P. J. Heron, *Nat. Commun.* **11**, 1 (2020).
- [42] I. Neudecker, K. Perzlmaier, F. Hoffmann, G. Woltersdorf, M. Buess, D. Weiss, and C. H. Back, *Phys. Rev. B* **73**, 134426 (2006).
- [43] J. Podbielski, F. Giesen, and D. Grundler, *Phys. Rev. Lett.* **96**, 167207 (2006).
- [44] S. Neusser, B. Botters, and D. Grundler, *Phys. Rev. B* **78**, 054406 (2008).
- [45] J. Chen, H. Wang, T. Hula, C. Liu, S. Liu, T. Liu, H. Jia, Q. Song, C. Guo, Y. Zhang, J. Z. J. Zhang, X. Han, D. Yu, M. Wu, H. Schultheiss, and H. Yu, *Nano Lett.* **21**, 6237 (2021).
- [46] D. Rueffer, *Magnetic states and spin-wave modes in single ferromagnetic nanotubes*, PhD thesis, EPFL (2014).
- [47] J. Jorzick, S. O. Demokritov, B. Hillebrands, M. Bailleul, C. Fermon, K. Y. Guslienko, A. N. Slavin, D. V. Berkov, and N. L. Gorn, *Phys. Rev. Lett.* **88**, 047204 (2002).
- [48] A. G. Gurevich and G. A. Melkov, *Magnetization oscillations and waves* (CRC Press, Boca Raton, 1996).

# Supplemental Material of Confined Spin Waves in Magneto-chiral Nanotubes with Axial and Circumferential Magnetization

Maria Carmen Giordano, Mohammad Hamdi, and Andrea Mucchietto  
*École Polytechnique Fédérale de Lausanne (EPFL), School of Engineering, Institute of Materials,  
Laboratory of Nanoscale Magnetic Materials and Magnonics, 1015 Lausanne, Switzerland*

Dirk Grundler\*  
*École Polytechnique Fédérale de Lausanne (EPFL), School of Engineering, Institute of Materials,  
Laboratory of Nanoscale Magnetic Materials and Magnonics, 1015 Lausanne, Switzerland and  
École Polytechnique Fédérale de Lausanne, School of Engineering,  
Institute of Electrical and Micro Engineering, 1015 Lausanne, Switzerland*

(Dated: January 30, 2023)

## I. METHODS

### A. Samples fabrication

Nanotubes were fabricated by coating, via a plasma enhanced atomic layer deposition (PE-ALD) process, the ferromagnetic permalloy  $\text{Ni}_{80}\text{Fe}_{20}$  (Py) onto GaAs nanowires (NWs) previously grown on Si (111) substrates in a molecular-beam epitaxy reactor as reported in Ref. S1. The PE-ALD process was performed in a hot wall Beneq TFS 200 ALD reactor as described in Ref. S2. The largest external diameter of the nanotube hexagon was measured by SEM micrography, assuming that the NT was lying on one of the hexagon facets. The internal diameter was estimated by subtracting twice the average thickness of the ferromagnetic coating, measured with TEM microscopy. The Py NTs were transferred through an isopropyl alcohol solution on a 4-inch Si(100) wafer covered with 200 nm thick  $\text{SiO}_2$  with pre-patterned gold alignment markers for the fabrication of integrated coplanar waveguides (CPWs). The metallic CPWs were prepared by electron beam lithography and a following evaporation of 5 nm Ti/ 120 nm Au film. The CPWs' dimensions were chosen to enable impedance matching. The signal line, having a width of  $2.6 \pm 0.1 \mu\text{m}$  was separated by gaps of  $1.7 \pm 0.1 \mu\text{m}$  width from the ground lines. The CPW was fabricated in a way that the signal line was parallel to the long axis of the NT, placed in one of the gaps.

### B. Spin waves excitation-detection scheme

Spin wave eigenmodes were detected via microfocus Brillouin light scattering ( $\mu$ -BLS) microscopy at room temperature [S3, S4]. The CPW was electrically connected via wire bonding and a printed circuit board to a signal generator (Anritsu MG3692C) applying current. The corresponding magnetic microwave field excited spin precession in the NT at a fixed frequency. The frequency was varied in a step-wise manner from 2.5 to 12.5 GHz. A monochromatic laser with a wavelength of 473 nm and power of 0.5 mW was focused on the top surface of the NT. The recorded BLS signal was proportional to the square of the amplitude of the dynamic magnetization at the position of the laser spot. The sample was mounted on a closed loop piezo-electrical stage which allowed a precise positioning of the NT. The power was such that spin precession was excited in the linear regime. A magnetic field was applied parallel to the NT long axis ( $\mathbf{z}$  axis) via a permanent magnet mounted on a translation stage. The magnitude of the magnetic field is adjusted by changing the distance between magnets and sample. For the experiment on the sample NT-s1 (NT-s2) the static field was swept from +90 mT to +10 mT in steps of 4 mT (8 mT), from +7 mT to -7 mT in steps of 7 mT and again from -10 mT to -90 mT in steps of 4 mT (8 mT). The field of  $|7|$  mT corresponds to the minimum distance of the permanent magnet. Zero field has been reached by removing the permanent magnet.

---

\* dirk.grundler@epfl.ch

### C. Micromagnetic simulations

Micromagnetic simulations using OOMMF [S5] were performed to obtain a microscopic insight into SW excitations in NTs. A bitmap containing the required hexagonal geometry of the NT cross section in xy-plane was imported into OOMMF. This hexagonal cross section was rotated along z-axis by 15 degree in order to distribute the systematic roughness due to pixelization on all facets of NTs as uniform as possible (see Figure S1). This cross section was

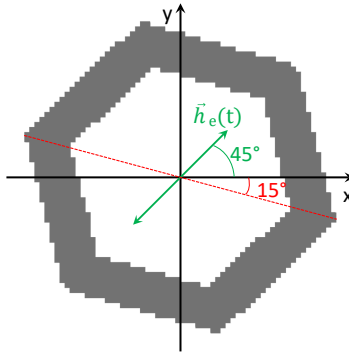


FIG. S1. NT cross section set as input for the micromagnetics simulations. The two ends of the NT are tilted at an angle of 15° with respect to xy-plane to emulate the irregular orientation of the defects in the measured NT. A spatially uniform sinc pulse  $\mathbf{h}_e$  is applied at 45° with respect to xy-plane. The geometry is discretized on a grid of 2.5 nm × 2.5 nm × 5 nm.

extended to  $L = 560$  nm as the length of the simulated NTs. The two ends of the NT is terminated at an angle of 15 degree with respect to xy-plane to emulate the irregular orientation of the defects in the measured NT. The geometry is discretized on a grid of 2.5 nm × 2.5 nm × 5 nm. A uniform DC magnetic field was applied along the z direction (NT axis), and equilibrium magnetization configuration was determined for each DC field value. Subsequently, a spatially uniform Sinc pulse of the form

$$\mathbf{h}_e = h_0 \left( \frac{\sin(2\pi f_c(t - t_0))}{2\pi f_c(t - t_0)} \right) [\cos(45^\circ) \hat{x} + \sin(45^\circ) \hat{y}] \quad (\text{S1})$$

with amplitude of  $h_0 = 2$  mT, cut-off frequency of  $f_c = 50$  GHz and  $t_0 = 500$  ps was applied at an angle of 45° in the xy-plane. A total simulation duration of  $T = 5$  ns was considered. The dynamic magnetization was recorded as a function of x, y, z every time step of  $\delta t = 5$  ps. A fast Fourier transformation (FFT) was performed on the magnetization of each pixel along the time axis to obtain the resonance spectrum. Then sums of power and phase of complex dynamic magnetization  $m_d = m_x + im_y$  were calculated to display the SW spatial profile for relevant frequencies.  $|m_d|$  was then integrated over the whole geometry (defined as PSD), and plotted as a function of frequency  $f$  in order to observe the microwave absorption. The input parameters used in the simulations were as follows: saturation magnetization  $M_s = 800$  kA/m, exchange constant  $A = 13$  pJ/m, and damping constant  $\alpha = 0.005$ . The dynamic magnetization profiles are visualized using "Mayavi: 3D Visualization of Scientific Data" [S6].

## II. SUPPLEMENTARY RESULTS

### A. BLS measurement on a second sample

The same BLS experiment has been performed on two individual Py NTs with the same scheme based on microwave excitation via a CPW antenna and  $\mu$ -BLS laser spin waves detection. Figure S2 shows the micrographs of the two samples. In Figure S3 the BLS spectra measured on the sample NT-s2 are reported as a function of the external applied field.

### B. Static micromagnetic simulations

In Figure S4 we report the results of the simulated static magnetization of a Py NT initially magnetized along its axis (z direction). The figure shows the magnetic hysteresis obtained by extracting the magnetization along z ( $M_z$ )

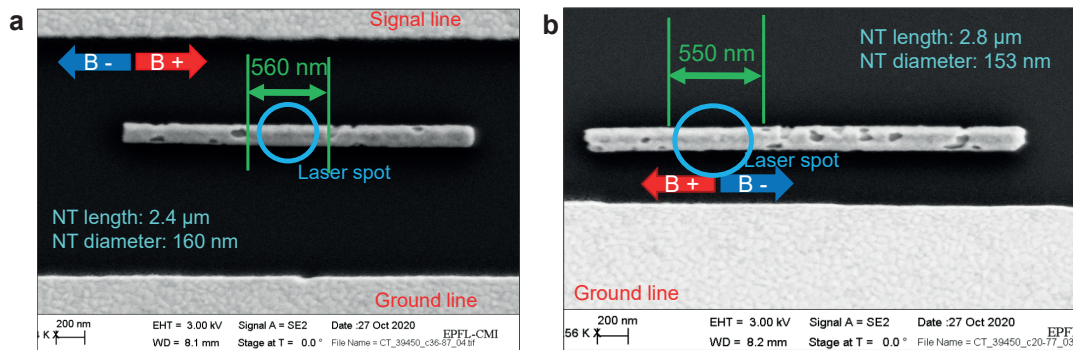


FIG. S2. Scanning electron microscopy images of (a) NT-s1 and (b) NT-s2. The relevant geometrical parameters are indicated on the picture and are summarized in Table II A. The BLS laser position and its diameter is approximately given by the blue circles depicted. Positive and negative direction of the external applied fields are depicted, respectively, with red and blue arrows.

TABLE S1. Geometrical parameters of the Py NTs investigated.

| Sample name       | Py shell thickness (nm) | External diameter $D_{out}$ (nm) | NT full length $l$ ( $\mu\text{m}$ ) | Distance between defects $L$ (nm) |
|-------------------|-------------------------|----------------------------------|--------------------------------------|-----------------------------------|
| NT-s1 (main text) | $22 \pm 1$              | $160 \pm 10$                     | $2.4 \pm 0.1$                        | $560 \pm 10$                      |
| NT-s2             | $22 \pm 1$              | $153 \pm 10$                     | $2.8 \pm 0.1$                        | $550 \pm 10$                      |

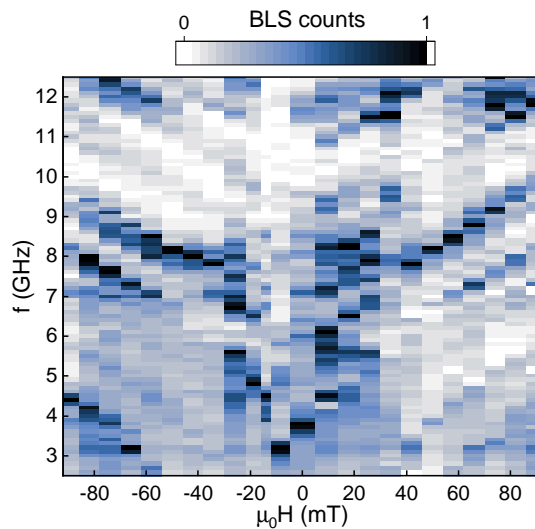


FIG. S3. BLS spectra detected at room temperature at the center of the sample NT-s2, plotted as a function of an external static magnetic field  $\mu_0 H$  applied along the NT axis.

as a function of the static magnetic field  $\mu_0 H_z$  along the same direction. The field was swept from positive to negative values (red curve) and from negative to positive values (blue curve). Depictions of the simulated NT magnetization are given at specific values of magnetic field selected on the red curve. For high positive magnetic fields  $\mu_0 H_z > 33$  mT a magnetic state approximated by a saturated state is found, where most of the spins are aligned along  $\mathbf{z}$ . The spin configuration is depicted for an applied field of 76 mT. Moving from high positive magnetic field towards zero, we observe that the relative magnetization stays at almost 1 until +33 mT and then drops to a value of 0.9 at +32 mT. At 32 mT the magnetization curls at the ends of the tube to minimize the stray field and remains axially in the center to minimize the exchange energy. The end-vortices show opposite chirality as expected for thick tubes with  $t/r_0 > 0.2$  [S7]. This magnetic configuration is known as the mixed state. With  $\mu_0 H_z$  decreasing from 32 mT to 0 mT,  $M_z/M_s$  is found to decrease monotonously down to 0.7. At  $\mu_0 H_z = 0$  the ground state is still the mixed state. The relative

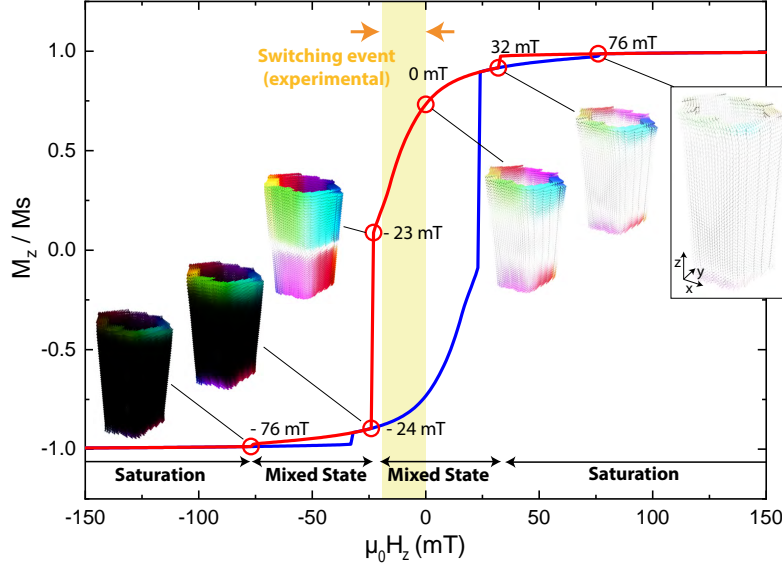


FIG. S4. Simulated static magnetization hysteresis of a Py NT magnetized along its axis ( $\mathbf{z}$  direction) when the field is swept from positive to negative values (red curve) and from negative to positive values (blue curve). Magnetic configurations are extracted from the simulations at specific fields and displayed for +76, +32, 0, -23, -24 and -76 mT.

magnetization reduces to zero for a magnetic field value of -23 mT. Here, the end-vortices having opposite senses of rotations, have expanded such that they are separated by a Néel-type domain wall located in the center. At -24 mT a switching event occurs whereby the central magnetization changes sign, leading to the formation of a mixed state with magnetization aligned along the negative  $\mathbf{z}$  axis in the central part of the nanotube approaching  $M_z/M_s = -0.9$ . The formation of the saturated magnetic state is observed starting from -76 mT. The magnetic field range where the BLS data suggest a decrease of relative NT magnetization terminating in a switching event (from 0 to -18 mT) is highlighted in yellow for comparison with the simulated hysteresis.

### C. Dynamic micromagnetic simulations

In Figure S5, we report the power spectral density (PSD), outcome of the dynamic micromagnetic simulations, as a function of an external applied field. The spectra shown in the main text of the manuscript are extracted from this 2D map at specific fields (+58 mT, 0 mT, -14 mT).

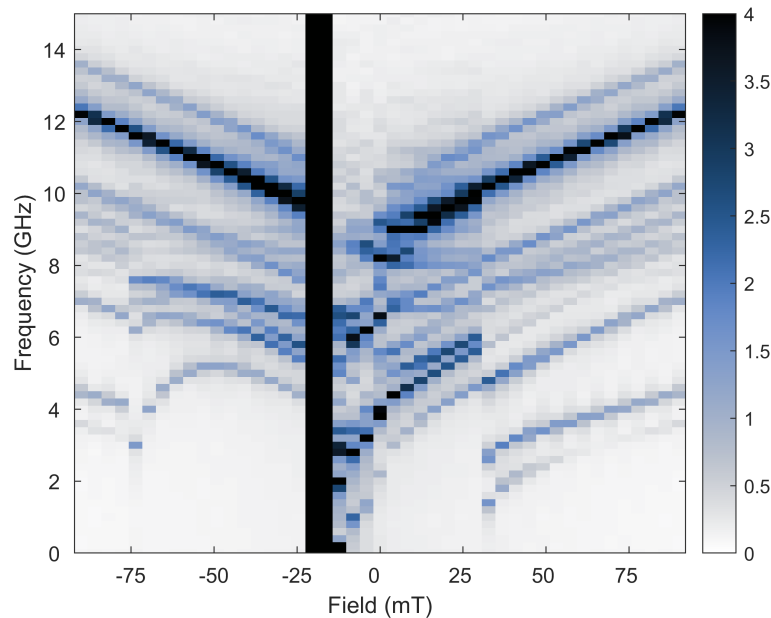


FIG. S5. Power spectral density (PSD), outcome of the dynamic micromagnetic simulations, as a function of an external applied field.

#### Contributions to this work

The first two authors M. C. Giordano and M. Hamdi contributed equally to this work.

#### References

- 
- [S1] F. Matteini, G. Tütüncüoğlu, D. Mikulik, J. Vukajlovic-Plestina, H. Potts, J.-B. Leran, W. C. Carter, and A. Fontcuberta i Morral, Impact of the Ga droplet wetting, morphology, and pinholes on the orientation of GaAs nanowires, *Crystal Growth & Design* **16**, 5781 (2016).
  - [S2] M. C. Giordano, S. Escobar Steinvall, S. Watanabe, A. Fontcuberta i Morral, and D. Grundler,  $\text{Ni}_{80}\text{Fe}_{20}$  nanotubes with optimized spintronic functionalities prepared by atomic layer deposition, *Nanoscale* **13**, 1351 (2021).
  - [S3] S. O. Demokritov and V. E. Demidov, Micro-Brillouin light scattering spectroscopy of magnetic nanostructures, *IEEE Trans. Magn.* **44**, 6–12 (2008).
  - [S4] T. Sebastian, K. Schultheiss, B. Obry, B. Hillebrands, and H. Schultheiss, Micro-focused Brillouin light scattering: imaging spin waves at the nanoscale, *Frontiers in Physics* **3**, 35 (2015).
  - [S5] M. J. Donahue and D. G. Porter, *OOMMF user's guide, version 1.0* (US Department of Commerce, National Institute of Standards and Technology, 1999).
  - [S6] P. Ramachandran and G. Varoquaux, Mayavi: 3D visualization of scientific data, *Computing in Science & Engineering* **13**, 40 (2011).
  - [S7] A. P. Chen, J. M. Gonzalez, and K. Y. Guslienko, Magnetization configurations and reversal of magnetic nanotubes with opposite chiralities of the end domains, *J. Appl. Phys.* **109**, 073923 (2011).